

A model supersonic buried-nozzle jet: instability and acoustic wave scattering and the far-field sound

Arnab Samanta^{1,†} and Jonathan B. Freund^{2,3}

¹Department of Aerospace Engineering, Indian Institute of Science, Bangalore 560012, India

²Department of Mechanical Science and Engineering, University of Illinois at Urbana–Champaign, Urbana, IL 61801, USA

³Department of Aerospace Engineering, University of Illinois at Urbana–Champaign, Urbana, IL 61801, USA

(Received 7 November 2014; revised 1 May 2015; accepted 21 June 2015)

We consider sound source mechanisms involving the acoustic and instability modes of dual-stream isothermal supersonic jets with the inner nozzle buried within an outer shroud-like nozzle. A particular focus is scattering into radiating sound waves at the shroud lip. For such jets, several families of acoustically coupled instability waves exist, beyond the regular vortical Kelvin–Helmholtz mode, with different shapes and propagation characteristics, which can therefore affect the character of the radiated sound. In our model, the coaxial shear layers are vortex sheets while the incident acoustic disturbances are the propagating shroud modes. The Wiener–Hopf method is used to compute their scattering at the sharp shroud edge to obtain the far-field radiation. The resulting far-field directivity quantifies the acoustic efficiency of different mechanisms, which is particularly important in the upstream direction, where the results show that the scattered sound is more intense than that radiated directly by the shear-layer modes.

Key words: acoustics, aeroacoustics

1. Introduction

The use of buried nozzles (see figure 1) in turbofan engines (e.g. the Rolls Royce RB211-535), where the outer fan cowling extends beyond the inner convergent nozzle, is thought to reduce jet noise because of the internal mixing between the hot core jet and the cooler bypass coflow from the fan before either of them interacts with the ambient flow (see e.g. Smith 2004). This reduced shear suppresses some of the acoustic sources, but the shear layer is similarly unstable to a spectrum of hydrodynamic Kelvin–Helmholtz (K–H)-like disturbances, which provide a reasonable model for the large-scale turbulence structures that are primary contributors to the far-field sound (Laufer & Yen 1983; Crighton & Huerre 1990; Tam, Golebiowski & Seiner 1996). Recent studies have demonstrated striking similarities between measured pressure fluctuations and those associated with wavepacket-like instabilities of the

† Email address for correspondence: samanta@aero.iisc.ernet.in

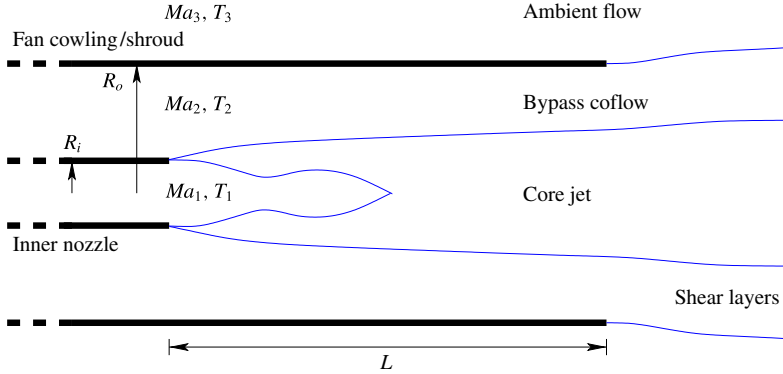


FIGURE 1. (Colour online) Schematic of the buried-nozzle configuration.

free shear-layer K–H mode, when measured just outside the shear layer (Jordan & Colonius 2013). The rotating turbofan also generates sound, which propagates upstream and downstream as duct modes. Such propagating modes do not radiate by themselves, but like the K–H modes can be scattered off the solid surfaces. Our model computes the acoustic efficiencies of both vortical modes, as a model for these large-scale structures, and acoustic modes, as a model for fan noise, as these are scattered off the sharp edge of the outer cowling.

The coflow arrangement suppresses radiation by shielding the ambient flow from the highest-speed unsteady disturbances of the core jet, which in turn reduces their acoustic radiation efficiency (see Papamoschou & Debiasi 2003). This effect can be particularly strong when the shear layers only support subsonic disturbances relative to the ambient. Low-bypass supersonic turbofans used in military aircraft usually have an afterburning section (e.g. Pratt and Whitney F100-PW-229, General Electric F110-GE-129), where the core and bypass flows intermix before they exhaust via a variable-area nozzle. Although radiated aerodynamic noise is sometimes considered to be of lesser importance to military engines, it is still a concern because of its role in aural injury, which can potentially deafen personnel. Likewise, if similar high-specific-thrust turbofans are ever to be used for commercial flight, it is important to understand their basic sound source mechanisms. In general, this configuration introduces sound mechanisms that can entail the scattering from both the solid edges (nozzle and fan cowling, see figure 1) plus the refraction due to flow non-uniformity. At sufficiently high speeds, scattering mechanisms might likewise include the additional families of instabilities as discussed below.

To investigate potential radiation mechanisms, we study the coflowing shrouded supersonic jet model shown in figure 2. It includes several of the sound mechanisms available in the configuration shown in figure 1, including the scattering of both hydrodynamic instability modes and the propagating shroud (duct) modes into acoustic radiation. Without the inner nozzle directly represented in our model, except as a source for the incident instability modes, we do not include its role in scattering, which is expected to be of secondary importance. The upstream-propagating reflected acoustic waves that could couple with the buried-nozzle lip are finite in number and, depending upon the core jet and bypass coflow conditions, most of them decay in the upstream direction (Samanta & Freund 2008). This will be particularly true for high-speed jets with low-speed coflows, as considered here. We also do not consider

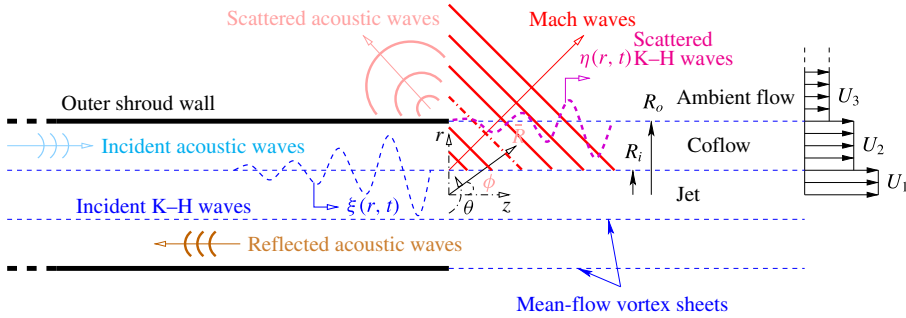


FIGURE 2. (Colour online) Schematic of the shroud with coflow.

any geometric details of the inner nozzle when calculating the amplitude functions in § 4.1, as the focus will be on the efficiencies of the respective scattering mechanisms by setting the net power of all incident waves to unity (see (4.1)).

The actual jets of interest are, of course, turbulent. However, physics-based (mostly linear) reduced-order models have provided mechanistic descriptions of key interactions. The qualitative similarity of the K–H instability waves of the inflectional free shear layer to the largest wave-like eddies of jet instabilities is well established (see e.g. Michalke 1972; Liu 1981; Ho & Huerre 1984), which has been utilised in noise models for turbulent jets (Crighton & Huerre 1990; Jordan & Colonius 2013).

Perfectly expanded free jets at sufficiently high speeds have characteristics without analogues in their lower-Mach-number counterparts. Supersonic jets, for example, support additional instabilities beyond K–H modes (e.g. Tam 1995), which suggests that the turbulent mixing noise can entail additional mechanisms depending upon the flow parameters. For compressible round jets, a vortex sheet model supports K–H waves and other types of unstable modes (Tam & Hu 1989), which arise via acoustic coupling across the jet core (Gill 1965). For given streamwise and azimuthal wavenumbers, these latter modes are unstable simultaneously with the K–H mode and are integral to the lip scattering problem that we consider. It is particularly noteworthy that for large enough Ma_1 , some of these supersonic instability mode(s) are predicted to grow faster (spatially) than the corresponding K–H mode (Luo & Sandham 1997). Thus, these modes, and the corresponding turbulent structures they model, are potentially important sources of far-field sound, which have not been studied in detail for the shrouded jet configuration we consider.

When fluctuations propagate with a supersonic convective Mach number, it is well understood that they can radiate efficiently as Mach waves, which form the dominant component of sound for supersonic jets. Mach-wave intensity decays super-algebraically outside a Mach cone, whose half-angle is $\cos^{-1}(a_\infty/v_j)$, where a_∞ is the ambient sound speed and v_j is the jet convective speed, so such radiation is effectively confined to aft angles. If $(Ma_1 - Ma_2) \gtrsim 2$ (see (3.1) for the precise expression), where Ma_2 is the coflow Mach number, unstable acoustically coupled supersonic modes are also unstable and likewise radiate Mach waves (see Tam & Hu 1989), augmenting the aft-angled radiation. Sideline and upstream acoustic radiation is less intense than downstream radiation, though it is important and has a less well-defined source mechanism (see e.g. Tam 2009). In addition to the unstable modes, in free jets there also exists a continuous spectrum of neutral modes with upstream-propagating subsonic phase speeds (the subsonic waves) (Tam & Hu 1989;

Nichols & Lele 2011), which scatter into radiating sound as we consider next. The modes supported by the shrouded jets we consider are classified in §3.

Imperfectly expanded supersonic jets generate strong screech tones radiating primarily upstream via interaction between the flow turbulence and the shock cells (e.g. Powell 1953; Harper-Bourne & Fisher 1973; Tam 1995; Shen & Tam 2002; Tam, Parrish & Viswanathan 2014). It is now well established that a type of feedback mechanism is responsible for these tones (Powell 1953), where the upstream-travelling acoustic waves play the important role of closing the feedback loop (Tam *et al.* 2014). The character of these acoustic waves and whether they propagate only in the subsonic coflow or in the core supersonic jet has yielded the two-screech-tone phenomenon investigated by Shen & Tam (2002). The upstream-propagating acoustic modes, which we consider in §4 for scattering and are classified in §3, are indeed of the second type where they propagate along the core supersonic jet. In supersonic jets with shock cells, these waves perturb the jet shear layer near the nozzle exit, thereby creating new instabilities of the core jet. In perfectly expanded supersonic jets as we consider here these waves could be the source of upstream and sideline radiation by allowing them to scatter at the shroud lip, whose possibility we investigate in this work. It should be noted that for the screech tones to sustain, the upstream acoustic waves must radiate fully upstream ($\sim 180^\circ$ to the jet axis) within a narrow band, while we show that the radiation via scattering is usually over a broader range of upstream but also at sideline angles, which is where the higher harmonics of screech tones also radiate (Tam *et al.* 2014).

The introduction of a solid surface – the semi-infinite shroud (see figure 2) – adds complexity by coupling all these free jet modes and the confined shroud modes. It also introduces a second family of K–H modes associated with the outer shear layer, which we shall see, for typical conditions, have higher growth rates than the corresponding core jet K–H modes. However, when the coflow is subsonic, as we consider, their phase speed will be subsonic and hence non-radiating, although they remain an essential component of the overall scattering mechanism. Since the aft radiation will be dominated by Mach waves, we can anticipate that it will be less sensitive to the introduction of the shroud *per se*, aside from its well-understood shielding effect (Papamoschou & Debiasi 2003). However, it is much harder to anticipate the sideline and upstream radiation, which in our model is expected to arise primarily from interactions with the shroud edge. In short, the shroud can allow otherwise non-radiating modes to radiate sound to the far field. The scattering of the unstable K–H and supersonic modes of the core jet is analysed in §4.1. We also consider both tonal and multimodal (broadband) modes as incident waves and study the corresponding radiation in §§4.2 and 4.3 respectively. Some comments on the nature of the acoustic source in all the cases considered are given in §4.4. The corresponding far field of each of the incident waves is discussed in §4.5. For all cases, we neglect mean swirl, which is known to support both discrete and continuous spectra hydrodynamic modes (Heaton & Peake 2006), different from the ones we consider.

Our analysis of cases with supersonic core flows, including the multiple classes of instability modes and their role in generating far-field sound, shares some features with configurations considered in the past. The simplest is scattering from an open shroud without mean flow (Levine & Schwinger 1948). Inclusion of flow and the instability waves it supports required the development of a Kutta condition to enable vortex shedding, which eventually facilitated an analysis of subsonic jet scattering in such configurations (Munt 1977, 1990). Centre bodies were later added to the configuration

(Taylor, Crighton & Cargill 1993; Gabard & Astley 2006), and the specific buried-nozzle configuration (figure 1) was first analysed in the low-frequency (plane wave) asymptotic limit by Taylor *et al.* (1993). This was extended by Samanta & Freund (2008) to include finite-frequency acoustic waves and core jet vortical waves, in order to analyse their role in scattering at the shroud exit, phenomenologically similar to that considered here. This suggested a stronger and possibly different radiation character even for subsonic core jets (see Samanta 2009). As in the present study, scattering at the inner nozzle was neglected, enabling an analytical solution using a scalar Wiener–Hopf method (see e.g. Noble 1988).

Inclusion of the inner nozzle scattering leads to a matrix Wiener–Hopf problem, which has been used by Veitch & Peake (2008) to study acoustic scattering from subsonic turbofan configurations for both buried and protruded nozzles. It was observed that for large separation L between the buried nozzle and the outer shroud (see figure 1), particularly when the outer shroud edge lies within a cone-of-influence of the inner instability wave, the effect of rescattering at the buried nozzle by the reflected acoustic modes is important, although there is always a minimum frequency ω below which the inner instability mode ceases to exist (Samanta & Freund 2008). Besides ω , the existence of reflected modes also depends upon $Ma_1 - Ma_2$ and R_i/R_o , and there are fewer reflected acoustic modes when $Ma_1 - Ma_2$ is large for a given ω and R_i/R_o combination (Samanta & Freund 2008). Thus, for $Ma_1 > 1$ considered here, it is anticipated that the reflected modes in the bypass stream will not be important (or even present), unless R_i/R_o is unrealistically small or for very large ω , near the corresponding cutoff frequency. Hence, we disregard rescattering at the buried nozzle. This is reaffirmed in §4.3 in the context of multimode scattering.

For configurations involving flow past a sharp trailing edge, a Kutta condition is needed to model the essentially viscous fluid mechanics in the neighbourhood of the singularity. A family of well-posed Kutta conditions are available for subsonic flows. These range from the full Kutta condition, where the vortex sheet leaves the edge at zero gradient, to the nominally no Kutta condition, when the same gradient is allowed to be infinite (see Orszag & Crow 1970). A corresponding vortex-shedding parameter (see (2.26)) can be used to parameterise the effect of the specific Kutta conditions, which we do in §4.6. This provides some idea of how the scattering process might be modified by changing the local shroud-edge geometry, although we do not consider any particular modifications in this study. In contrast, there is a unique Kutta condition available for the supersonic-core inner nozzle lip, described in §2.3, which has been shown to be unambiguously matched with the subsonic-coflow solution (Morgan 1974; Peake 1994). The supersonic Kutta condition will be imposed to fix the amplitudes of K–H and supersonic instability modes in §4.1 via scattering of duct modes at the inner nozzle lip.

2. Problem definition

2.1. Governing equations

The inviscid non-thermal-conductive compressible-fluid flow equations

$$\frac{D\rho}{Dt} = -\rho \nabla \cdot \mathbf{u}, \quad (2.1a)$$

$$\rho \frac{D\mathbf{u}}{Dt} = -\nabla p, \quad (2.1b)$$

$$\frac{Ds}{Dt} = 0, \quad (2.1c)$$

support three types of linear disturbances: acoustic, vortical and entropy waves for uniform mean (e.g. Chu & Kovasznay 1957), where the entropy s is related to the pressure p and density ρ as $s = c_v \log(p/\rho^\gamma)$, with c_v the specific heat at constant volume and γ the specific heat ratio. Equation (2.1b) also corresponds to $D\boldsymbol{\Omega}/Dt = 0$, if the flow is barotropic, for vorticity $\boldsymbol{\Omega} = \nabla \times \mathbf{u}$ and uniform mean as considered here. Decomposing $\mathbf{q} = [\mathbf{u} \ \rho \ s]^\top$ into a uniform mean and perturbation as $\mathbf{q} = \bar{\mathbf{q}} + \mathbf{q}'(\mathbf{x}, t)$ for $\bar{\mathbf{q}} = [\bar{u}_z \mathbf{e}_z \ \bar{\rho} \ \bar{s}]^\top$ yields the linearised perturbation equations

$$\left(\frac{\partial}{\partial t} + \bar{u}_z \frac{\partial}{\partial z} \right) \rho' = -\bar{\rho} \nabla \cdot \mathbf{u}', \quad (2.2a)$$

$$\bar{\rho} \left(\frac{\partial}{\partial t} + \bar{u}_z \frac{\partial}{\partial z} \right) \mathbf{u}' = -\nabla p', \quad (2.2b)$$

$$\left(\frac{\partial}{\partial t} + \bar{u}_z \frac{\partial}{\partial z} \right) (p' - \bar{c}^2 \rho') = 0. \quad (2.2c)$$

In forming (2.2c), we have used $s' = (p' - \bar{c}^2 \rho')$, with $\bar{c} = \sqrt{\gamma \bar{p} / \bar{\rho}}$ being the speed of sound. Equations (2.2a)–(2.2c) are combined to obtain the familiar advected wave equation

$$\left(\frac{\partial}{\partial t} + \bar{u}_z \frac{\partial}{\partial z} \right)^2 p - \bar{c}^2 \nabla^2 p = 0. \quad (2.3)$$

For the piecewise-uniform flow that we assume, these wave-like disturbances are unambiguously defined in each of the substreams, but couple only at the boundaries. We focus on the acoustic and vorticity wave solutions, particularly how they are linked via the vortex sheet and the sharp edge of the shroud, while neglecting the role of entropy wave scattering. Entropy waves are generated because of temperature (entropy) fluctuations, which could be supported for heated core jets, not considered here. However, unless such temperature fluctuations are comparable to those actually inside a typical combustion chamber or there is condensation during jet mixing, the entropy–acoustic and entropy–vorticity interactions are unlikely to result in a source of radiated sound comparable to the interactions we consider (e.g. Hirschberg & Hoeijmakers 2014).

2.2. Model configuration

The model shroud is a semi-infinite ($-\infty < z < 0$) circular cylinder of radius R_o , as shown in figure 2. It is rigid, impermeable and of negligible thickness. The three-stream mean flow \bar{u}_z is

$$\bar{u}_z = \begin{cases} U_1 & \text{for } r < R_i, \\ U_2 & \text{for } R_i < r < R_o, \\ U_3 & \text{for } r > R_o, \end{cases} \quad (2.4)$$

where R_i is the radius of the core jet. The core jet temperature T_1 is typically much larger than both that of the coflow T_2 and that of the ambient flow T_3 , which for convenience we set equal, $T_2 = T_3 = T_o$, and define $\kappa_T = \sqrt{T_1/T_o}$. Similarly, the density of the core jet ρ_1 may be independently related through a second independent parameter $\kappa_\rho = \rho_1/\rho_o$ to the outer flows, where $\rho_2 = \rho_3 = \rho_o$. In this work, we have assumed $\kappa_T = \kappa_\rho = 1$ everywhere, except in figure 3(c), where we briefly highlight the effect of core jet heating on the modal spectra. Detailed interactions from heated

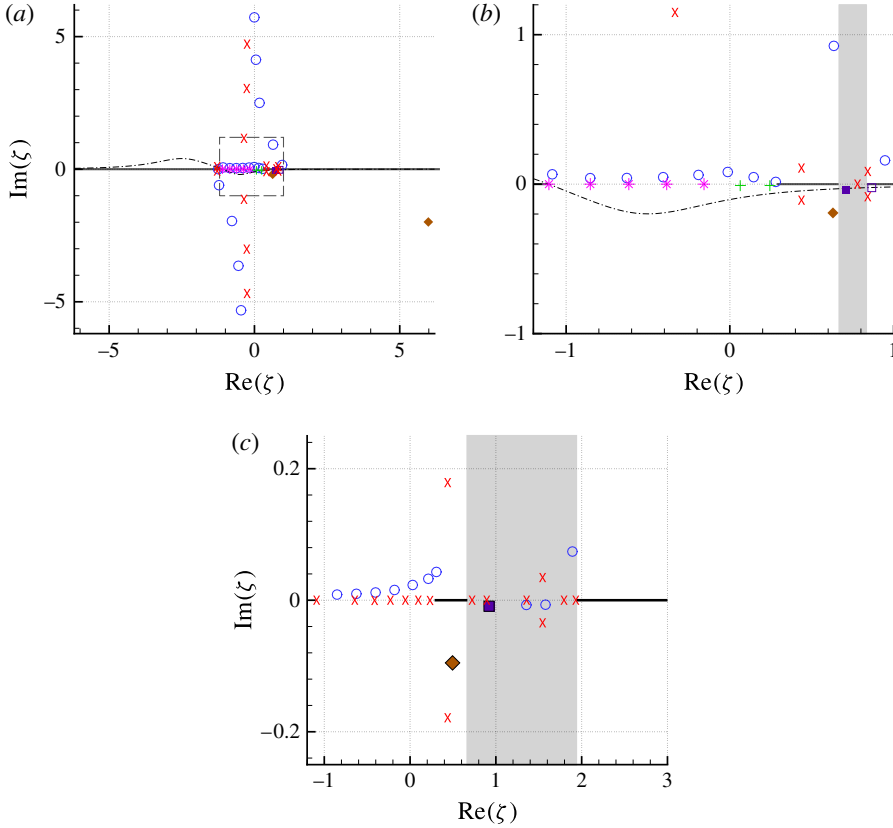


FIGURE 3. (Colour online) The zeros (○) and poles (×) of the kernel (2.22) for $Ma_1 = 2.5$, $Ma_2 = 0.2$, $Ma_3 = 0.1$, $R = 0.75$, $\omega = 8$ and $m = 0$. For (a,b) $\kappa_T = 1$, with the latter being the region shown within the box in (a), and for (c) $\kappa_T = 3.16$. The specific modes are ◆ K–H; ■ supersonic instability $n = 1$; □ supersonic instability $n = 2$; * upstream-phase speed neutral; and + downstream-phase speed neutral (see text). The line - - - - is the integration contour of (2.25) and the shaded region shown in (b) satisfies (3.1). The thick horizontal lines are the branch cuts.

core jets could be a subject for future study, but we have retained κ_T and κ_ρ in the formulation for generality. Quantities are non-dimensionalised by R_o , T_1 , ρ_1 and U_1 , which yield Mach numbers $Ma_j = U_j/\bar{c}_1$ for $j = 1, 2, 3$ and the non-dimensional inner jet radius $R = R_i/R_o$, where \bar{c}_1 is the core jet acoustic speed. The core jet is assumed to be supersonic ($Ma_1 > 1$), while the outer flows are subsonic ($Ma_{2,3} < 1$). With this non-dimensionalisation and the introduction of a velocity potential $\phi_t(r, \theta, z)$ such that $\mathbf{u} = \nabla\phi_t$, (2.3) becomes

$$\left(\frac{\partial}{\partial t} + Ma_1 \frac{\partial}{\partial z}\right)^2 \phi_t - \Delta\phi_t = 0, \quad r < R, \tag{2.5a}$$

$$\kappa_T^2 \left(\frac{\partial}{\partial t} + Ma_2 \frac{\partial}{\partial z}\right)^2 \phi_t - \Delta\phi_t = 0, \quad R < r < 1, \tag{2.5b}$$

$$\kappa_T^2 \left(\frac{\partial}{\partial t} + Ma_3 \frac{\partial}{\partial z}\right)^2 \phi_t - \Delta\phi_t = 0, \quad r > 1, \tag{2.5c}$$

where, for convenience, the non-dimensional lengths and time are expressed by their corresponding dimensional symbols. In forming (2.5), the pressure in each stream is

$$p_j = - \left(\frac{\partial \phi}{\partial t} + Ma_j \frac{\partial \phi}{\partial z} \right), \quad (2.6)$$

for $j = 1, 2, 3$, per the linearised unsteady Bernoulli equation. The subscript t indicates the total field, which will be constructed as a linear superposition of the incident and scattered fields.

2.3. Boundary and matching conditions

The non-penetration condition corresponds to zero normal velocity on the shroud:

$$\frac{\partial \phi_t}{\partial r}(1^-, \theta, z) = \frac{\partial \phi_t}{\partial r}(1^+, \theta, z) = 0, \quad z \leq 0. \quad (2.7)$$

Each of the vortex sheets must satisfy the usual kinematic and dynamic conditions. For the outer vortex sheet, linearised kinematic continuity yields

$$\left(\frac{\partial}{\partial t} + Ma_2 \frac{\partial}{\partial z} \right) \eta(\theta, z) = \frac{\partial \phi_t}{\partial r}(1^-, \theta, z), \quad z > 0, \quad (2.8)$$

$$\left(\frac{\partial}{\partial t} + Ma_3 \frac{\partial}{\partial z} \right) \eta(\theta, z) = \frac{\partial \phi_t}{\partial r}(1^+, \theta, z), \quad z > 0, \quad (2.9)$$

where $\eta(\theta, z)$ is the radial displacement of the vortex sheet. Similarly, dynamic pressure continuity gives

$$\left(\frac{\partial}{\partial t} + Ma_2 \frac{\partial}{\partial z} \right) \phi_t(1^-, \theta, z, t) = \left(\frac{\partial}{\partial t} + Ma_3 \frac{\partial}{\partial z} \right) \phi_t(1^+, \theta, z, t), \quad z > 0. \quad (2.10)$$

The corresponding kinematic and dynamic boundary conditions on the inner vortex sheet are respectively

$$\left(\frac{\partial}{\partial t} + Ma_1 \frac{\partial}{\partial z} \right) \xi(\theta, z) = \frac{\partial \phi_t}{\partial r}(R^-, \theta, z), \quad -\infty < z < \infty, \quad (2.11)$$

$$\left(\frac{\partial}{\partial t} + Ma_2 \frac{\partial}{\partial z} \right) \xi(\theta, z) = \frac{\partial \phi_t}{\partial r}(R^+, \theta, z), \quad -\infty < z < \infty, \quad (2.12)$$

where $\xi(\theta, z)$ is the radial displacement of the inner sheet from $r = R$, and

$$\kappa_\rho \left(\frac{\partial}{\partial t} + Ma_1 \frac{\partial}{\partial z} \right) \phi_t(R^-, \theta, z, t) = \left(\frac{\partial}{\partial t} + Ma_2 \frac{\partial}{\partial z} \right) \phi_t(R^+, \theta, z, t), \quad -\infty < z < \infty. \quad (2.13)$$

Imposition of the Kutta condition entails setting $\partial \eta / \partial z$ at the shroud edge ($r = 1, z = 0$) (Orszag & Crow 1970). There is a family of acceptable asymptotic behaviours for $\eta(z)$ that provide this condition. Taking $\eta \sim z^{3/2}$ corresponds to the full Kutta condition, for which the vortex sheet leaves with $\partial \eta / \partial z = 0$. At the other extreme, $\eta \sim z^{1/2}$ implies that the vortex sheet leaves such that $\partial \eta / \partial z \rightarrow \infty$, which is the nominal no Kutta condition. Since the particular Kutta condition mediates the vortex scattering from the lip, we follow Rienstra (1984) and define a complex

vortex-shedding parameter α (see (2.26)), such that $0 < |\alpha| < 1$, to compute the results of § 4.6. We use α to assess the role of specific shroud-edge conditions on the scattered noise. Setting $\alpha = 0$ suppresses vortex shedding, while $\alpha = 1$ can be considered to be the full-vortex-shedding case, also ensuring pressure to be finite at the edge. Supersonic flow requires $\eta \sim z$ (Peake 1994), which we use to compute the incident vortical perturbation in § 4.1.

A radiation condition is needed to ensure that all acoustic waves are outgoing and appropriately decay at large distances. A causality criterion enforces the necessary radiation condition (Crighton & Leppington 1974; Jones & Morgan 1974). For the selected harmonic time dependence $\exp(-i\omega t)$, with complex $\omega = \omega_r + i\omega_i$, causality requires $\omega_i \geq 0$. Alternatively, for $\omega = |\omega| \exp(i\delta)$, the corresponding requirement is $0 \leq \delta \leq \pi/2$. When ω_i is largest (i.e. $\delta \rightarrow \pi/2$), the radiation condition is thus satisfied and the integration contour Γ (see (2.25)) is best chosen at this mathematical limit, with solutions for real $\omega_i \rightarrow 0$ (the physical limit) as $\delta \rightarrow 0$ obtained via analytic continuation. Instability modes such as K–H and the supersonic instability modes need to be handled with care as the deformation of Γ is not possible as these modes exhibit unbounded maximum temporal growth (e.g. Brambley 2009a). Instead, we simply factor out these modes following a procedure detailed in Samanta & Freund (2008), which results in Fourier integrals (see 2.25) that are now convergent, and at the same time the above causality procedure becomes feasible. The instability modes are calculated separately using residue theorem (see 2.28) and added to the integral solutions.

2.4. Solution overview

The corresponding analysis for subsonic $Ma_1 < 1$ flow with $\kappa_T = \kappa_\rho = 1$ is reported elsewhere (see Samanta & Freund 2008; Samanta 2009) and follows in many ways the approaches of Munt (1977), Rienstra (1984), Munt (1990), Taylor *et al.* (1993) and Gabard & Astley (2006). Therefore, we focus here on the necessary changes for the new supersonic flow configurations.

2.4.1. Near-field Wiener–Hopf solutions

Equations (2.5)–(2.13) are transformed using

$$\begin{aligned} \hat{q}^\pm(r, \zeta) \exp\{i(m\theta - \omega t)\} &= \int_{-\infty}^{+\infty} q(r, \theta, z, t) H(\pm z) \exp(-i\omega\zeta z) dz \\ &= \exp\{i(m\theta - \omega t)\} \int_{-\infty}^{+\infty} \tilde{q}(r, z) H(\pm z) \exp(-i\omega\zeta z) dz, \end{aligned} \tag{2.14}$$

where q is ϕ_r , η or ξ , while ζ is the Fourier transform of z in the frequency space. This operation is a half-range Fourier transform of q , with $H(z)$ being the Heaviside step function. The corresponding inverse transform is

$$\tilde{q}(r, z) = \frac{\omega}{2\pi} \int_{-\infty}^{+\infty} \hat{q}(r, \zeta) \exp(i\omega\zeta z) d\zeta. \tag{2.15}$$

The total potential $\tilde{\phi}_t$ is decomposed as

$$\tilde{\phi}_t = \tilde{\phi}_i + \tilde{\phi}, \tag{2.16}$$

where the incident disturbance

$$\tilde{\phi}_i(r, z) = \sum_{m=-\infty}^{\infty} \sum_{n=1}^{\infty} B_{mn}^+ \Psi_{mn}(r) \exp(i\mu_{mn}^+ \omega z) \quad (2.17)$$

is composed of right ‘+’ running waves, with m and n being the azimuthal and radial wavenumber indices respectively. The mode shape $\Psi_{mn}(r)$ and the axial wavenumber μ_{mn}^+ correspond to the shroud mode acoustic and jet vorticity solutions (Samanta & Freund 2008), with the amplitude B_{mn}^+ chosen for convenience such that the net incident acoustic wave power is unity. Single tone variants of (2.17) will also be considered.

Applying (2.14) to (2.5a)–(2.5c) yields three Bessel equations for the scattered $\hat{\phi}$:

$$\frac{1}{r} \frac{\partial}{\partial r} \left(r \frac{\partial \hat{\phi}}{\partial r} \right) + \left(\omega^2 \lambda_1^2 - \frac{m^2}{r^2} \right) \hat{\phi} = 0 \quad \text{for } r < R, \quad (2.18a)$$

$$\frac{1}{r} \frac{\partial}{\partial r} \left(r \frac{\partial \hat{\phi}}{\partial r} \right) + \left(\omega^2 \lambda_2^2 - \frac{m^2}{r^2} \right) \hat{\phi} = 0 \quad \text{for } R < r < 1, \quad (2.18b)$$

$$\frac{1}{r} \frac{\partial}{\partial r} \left(r \frac{\partial \hat{\phi}}{\partial r} \right) + \left(\omega^2 \lambda_3^2 - \frac{m^2}{r^2} \right) \hat{\phi} = 0 \quad \text{for } r > 1, \quad (2.18c)$$

where the radial wavenumbers are $\lambda_p = \lambda_p^+ \lambda_p^-$, with

$$\lambda_1^\pm = [1 - \zeta(Ma_1 \pm 1)]^{1/2}, \quad (2.19a)$$

$$\lambda_p^\pm = [\kappa_T - \zeta(\kappa_T Ma_p \pm 1)]^{1/2} \quad \text{for } p = 2, 3. \quad (2.19b)$$

The principal branch cuts must satisfy $\text{Im}[\lambda_p] > 0$ as $\zeta \rightarrow \infty$ per the causality condition discussed in § 2.3. This is ensured by the finite branch points at

$$\zeta_1^\pm = 1/(Ma_1 \pm 1), \quad (2.20a)$$

$$\zeta_p^\pm = \kappa_T/(\kappa_T Ma_p \pm 1) \quad \text{for } p = 2, 3. \quad (2.20b)$$

The domain of regularity of the transformed functions, which is a key step of the Wiener–Hopf analysis and is discussed for the corresponding subsonic flow by Samanta & Freund (2008), is a strip S formed by the intersection of three substrips where each of the $\text{Im}[\lambda_p] > 0$.

The transformed governing equations and boundary conditions are manipulated to form the Wiener–Hopf equation,

$$K(\zeta) \hat{\eta}^+(\zeta) - \hat{p}_o^+(\zeta) = \hat{p}_o^-(\zeta), \quad (2.21)$$

where $\hat{p}_o^+(\zeta)$ is the transformed (scattered) pressure jump across the outer vortex sheet, $\hat{p}_o^-(\zeta)$ is the corresponding jump across the shroud wall and $K(\zeta)$ is the Wiener–Hopf kernel

$$K(\zeta) = \omega \left\{ \frac{(1 - \zeta Ma_2)^2}{\lambda_2} \left[\frac{H_m^{(1)}(\lambda_2 \omega) + V(\zeta) J_m(\lambda_2 \omega)}{H_m^{(1)'}(\lambda_2 \omega) + V(\zeta) J_m'(\lambda_2 \omega)} \right] - \frac{(1 - \zeta Ma_3)^2}{\lambda_3} \frac{H_m^{(1)}(\lambda_3 \omega)}{H_m^{(1)'}(\lambda_3 \omega)} \right\}, \quad (2.22)$$

where

$$V(\zeta) = \frac{\lambda(\zeta)J_m(\lambda_1\omega h)H_m^{(1)'}(\lambda_2\omega h) - H_m^{(1)}(\lambda_2\omega h)J_m'(\lambda_1\omega h)}{J_m(\lambda_2\omega h)J_m'(\lambda_1\omega h) - \lambda(\zeta)J_m(\lambda_1\omega h)J_m(\lambda_2\omega h)} \quad (2.23)$$

and

$$\lambda(\zeta) = \kappa_\rho \frac{\lambda_2 (1 - \zeta Ma_1)^2}{\lambda_1 (1 - \zeta Ma_2)^2}. \quad (2.24)$$

These lead to the scattered pressure $\tilde{p}(r, z)$ in the three streams:

$$\tilde{p}(r, z) = \begin{cases} \frac{\omega^2}{2\pi} \int_\Gamma \frac{(1 - \zeta Ma_2)^2}{\lambda_2} T_1(r, \zeta) \hat{\eta}^+(\zeta) \exp(i\omega\zeta z) d\zeta, & r < R, \\ \frac{\omega^2}{2\pi} \int_\Gamma \frac{(1 - \zeta Ma_2)^2}{\lambda_2} T_2(r, \zeta) \hat{\eta}^+(\zeta) \exp(i\omega\zeta z) d\zeta, & R < r < 1, \\ \frac{\omega^2}{2\pi} \int_\Gamma \frac{(1 - \zeta Ma_3)^2}{\lambda_3} T_3(r, \zeta) \hat{\eta}^+(\zeta) \exp(i\omega\zeta z) d\zeta, & r > 1, \end{cases} \quad (2.25)$$

where Γ is a suitable inverse transform contour through the strip S , the transformed vortex sheet displacement is

$$\hat{\eta}^+(\zeta) = B_{mn}^+ \bar{\Psi}_{mn} \frac{1 - \mu_{mn}^+ Ma_2}{(\mu_{mn}^+ - \zeta_{z1}) \hat{K}^- (\mu_{mn}^+) \hat{K}^+(\zeta) U(\zeta)} \left(\frac{\zeta - \zeta_{z1}}{\mu_{mn}^+ - \zeta} + \alpha \right) \quad (2.26)$$

and

$$T_1(r, \zeta) = \frac{J_m(\lambda_1\omega r) H_m^{(1)}(\lambda_2\omega h) + V(\zeta)J_m(\lambda_2\omega h)}{J_m(\lambda_1\omega h) H_m^{(1)'}(\lambda_2\omega) + V(\zeta)J_m'(\lambda_2\omega)}, \quad (2.27a)$$

$$T_2(r, \zeta) = \frac{H_m^{(1)}(\lambda_2\omega r) + V(\zeta)J_m(\lambda_2\omega r)}{H_m^{(1)'}(\lambda_2\omega) + V(\zeta)J_m'(\lambda_2\omega)}, \quad (2.27b)$$

$$T_3(r, \zeta) = \frac{H_m^{(1)}(\lambda_3\omega r)}{H_m^{(1)'}(\lambda_3\omega)}, \quad (2.27c)$$

with $\bar{\Psi}_{mn} = \Psi_{mn}(r = 1)$.

The kernel split functions \hat{K}^+ and \hat{K}^- of (2.26) are obtained following an established procedure for scalar Wiener–Hopf kernels, discussed in our previous work (Samanta & Freund 2008). Contributions from a specific zero ζ' of (2.22), especially those corresponding to the instability waves, are introduced to (2.25) via residue theorem:

$$\begin{aligned} \tilde{p}_{res}(r, z) &= i\omega^2 \sum_{\zeta'} \exp(i\omega\zeta' z) \lim_{\zeta \rightarrow \zeta'} [\hat{\eta}^+(\zeta)] \\ &\times H(z) \begin{cases} (1 - \zeta' Ma_2)^2 \lim_{\zeta \rightarrow \zeta'} [T_1(r, \zeta)/\lambda_2], & r < R, \\ (1 - \zeta' Ma_2)^2 \lim_{\zeta \rightarrow \zeta'} [T_2(r, \zeta)/\lambda_2], & R < r < 1, \\ (1 - \zeta' Ma_3)^2 \lim_{\zeta \rightarrow \zeta'} [T_3(r, \zeta)/\lambda_3], & r > 1, \end{cases} \quad (2.28) \end{aligned}$$

where

$$\lim_{\substack{\zeta \rightarrow \zeta' \\ \zeta_{ij} \neq \zeta'}} [\hat{\eta}^+(\zeta)] = B_{mn}^+ \bar{\Psi}_{mn} \frac{(1 - \mu_{mn}^+ Ma_2) \sum_j (\zeta' - \zeta_{pj})}{(\mu_{mn}^+ - \zeta') \hat{K}^- (\mu_{mn}^+) \hat{K}^+(\zeta') \sum_i (\zeta' - \zeta_{zi})}. \quad (2.29)$$

Here, ζ_{zi} and ζ_{pj} are respectively the i th zero and j th pole of $K(\zeta)$. The total pressure \tilde{p}_t is obtained by addition of the incident field \tilde{p}_i . It should be noted that (2.25) yields the scattered pressure from a single incident mode of wavenumber μ_{mm}^+ . For general multimode incident waves such single-mode solutions are summed per (2.17).

The form of (2.25) is checked following procedures we have used previously (Samanta 2009). In particular, this includes confirming that in the limit of $Ma_2 \rightarrow Ma_1$, the present analytical solutions degenerate to that of Munt (1977). Furthermore, numerical evaluations of (2.25) are substituted back into a finite-difference approximation of (2.5) and (2.7)–(2.13) to ensure that they are indeed solutions of these equations to the known accuracy of the corresponding finite-difference approximation and up to the specified tolerance of the corresponding numerical integration.

Numerical evaluation of (2.25) requires significant care. To ensure analytic continuity, the kernel split function contour C to evaluate the split functions of (2.22) and the inverse transform contour Γ of (2.25) need to be chosen after inspection of the spectrum of zeros and poles for a particular kernel. The kernel split functions are computed via a standard formula for scalar kernels (e.g. Noble 1988), which needs to be evaluated once for the entire flow field and a given set of parameters. However, on numerical refinement it was observed that the scattered pressure (2.25) is sensitive to its numerical accuracy and limit. Since the integrands have relatively localised regions with high gradients, it is efficient to use an adaptive quadrature scheme, for which we selected a target tolerance of 10^{-5} , which was confirmed to be more than adequate (see Samanta 2009). The numerical limits of the kernel integral are taken to be 10^3 times the corresponding inverse transform contour Γ limits of (2.25). The inversion contour needs to be computed for each (r, z) pair but for a given set of contour points, which is done via a trapezoidal algorithm, with the results confirmed to be insensitive to the number of quadrature points, typically approximately 1000. Asymptotic forms of the functions in (2.22) are used as appropriate during the numerical evaluation to achieve faster and accurate convergence of the respective integrands.

2.4.2. Far-field solutions

For the acoustic far field, we seek large- r solutions in spherical coordinates (\bar{R}, Φ) centred at $r = 0$ on the $z = 0$ shroud exit plane, with $z = \bar{R} \cos \Phi$ and $r = \bar{R} \sin \Phi$. Specifically, this amounts to evaluating (2.25) for $r > 1$ in the $\omega \bar{R} \rightarrow \infty$ limit.

Transforming (2.25) to spherical coordinates using (2.27c) yields

$$\tilde{p}(\bar{R}, \Phi) = \frac{\omega^2}{2\pi} \int_{\Gamma} \frac{(1 - \zeta Ma_3)^2}{\lambda_3} \frac{H_m^{(1)}(\lambda_3 \omega \bar{R} \sin \Phi)}{H_m^{(1)'}(\lambda_3 \omega)} \hat{\eta}^+(\zeta) \exp(i\omega \zeta \bar{R} \cos \Phi) d\zeta. \quad (2.30)$$

Here, $\Phi \in (0, \pi)$ and $\lambda_3(\zeta) \neq 0$, since Γ does not intersect the branch points ζ_3^{\pm} defined in (2.20). As $\omega \bar{R} \rightarrow \infty$, the asymptotic form of the Hankel function (see e.g. Abramowitz & Stegun 1964) allows (2.30) to be approximated as

$$\tilde{p} = \int_{\Gamma} G(\zeta) \exp\{\omega \bar{R} g(\zeta)\} d\zeta, \quad (2.31)$$

where

$$G(\zeta) \equiv \frac{\omega^2}{2\pi} \exp \left[- \left(\frac{m}{2} + \frac{1}{4} \right) i\pi \right] \frac{(1 - \zeta Ma_3)^2}{\lambda_3(\zeta)} \frac{\hat{\eta}^+(\zeta)}{H_m^{(1)'}(\lambda_3 \omega)} \left(\frac{2}{\pi} \frac{1}{\lambda_3 \omega \bar{R} \sin \Phi} \right)^{1/2}, \quad (2.32a)$$

$$g(\zeta) \equiv i[\lambda_3(\zeta) \sin \Phi + \zeta \cos \Phi]. \quad (2.32b)$$

It should be noted that these are analytic in the region containing Γ . As formulated, the asymptotic form of (2.31) can be found using the method of steepest descents. The saddle point(s) of $g(\zeta)$ are

$$\zeta_o = \frac{\kappa_T \cos \Theta - \kappa_T^2 Ma_3}{1 - \kappa_T^2 Ma_3^2}, \quad (2.33)$$

where

$$\Theta = \tan^{-1} \left(\sqrt{1 - \kappa_T^2 Ma_3^2} \tan \Phi \right). \quad (2.34)$$

An identical saddle point was also obtained by Munt (1977) and Gabard & Astley (2006) for different configurations, which is not surprising since the exponential variation of acoustic pressure outside the shroud is the same in those corresponding cases. The steepest descent directions are

$$\theta_0 = \pi/4 \quad \text{and} \quad \theta_1 = -3\pi/4. \quad (2.35a,b)$$

With this approach, the asymptotic form of (2.31) is

$$\begin{aligned} \tilde{p}_{asm}(\bar{R}, \Phi) &= \frac{\omega(1 - \zeta_o Ma_3)^2 \hat{\eta}^+(\zeta_o)}{\pi \bar{R} H_m^{(1)'}[\kappa_T \omega \sin \Phi / (1 - \kappa_T^2 Ma_3^2 \sin^2 \Phi)^{1/2}] \kappa_T \sin \Phi} \\ &\times \exp \left[i\omega \bar{R} \Gamma(\Phi) - im \frac{\pi}{2} \right] \quad \text{as } \omega \bar{R} \rightarrow \infty, \end{aligned} \quad (2.36)$$

with

$$\Gamma(\Phi) = \frac{\kappa_T \sqrt{1 - \kappa_T^2 Ma_3^2 \sin^2 \Phi} - \kappa_T^2 Ma_3 \cos \Phi}{1 - \kappa_T^2 Ma_3^2}. \quad (2.37)$$

It should be noted that (2.36) only includes the radiating part of the acoustic modes. The spatially growing modes, which include the shear-layer vorticity modes and the supersonic instability modes, continue to grow downstream, but are not our primary interest. In actual jets these growing modes eventually show finite-amplitude nonlinear effects, become decorrelated and decay amongst the ever larger turbulent scales downstream. It is therefore justified to ignore their influence on the far-field asymptotic solutions by closing the respective integration contours (of (2.36)) such that the spatially growing modes are excluded. Still, it is important to ascertain at what directivity angles these growing modes can be expected to be dominant. Towards this, the same coordinate transformations are applied to the $r > 1$ solution of (2.28) to yield a condition that ensures the decay of these waves in any Φ direction:

$$\text{Im}[\lambda_3(\zeta') \sin \Phi + \zeta' \cos \Phi] \geq 0. \quad (2.38)$$

On using (2.19), we see that the smallest Φ at which p_{res} starts to decay exponentially is

$$\Phi^* = \tan^{-1} \left[- \frac{\text{Im}(\zeta')}{\text{Im}[\kappa_T^2 (1 - \zeta' Ma_3)^2 - \zeta'^2]^{1/2}} \right], \quad (2.39)$$

where ζ' is the zero of the corresponding spatially growing modes as classified in § 3. We use Φ^* in § 4.5 to identify where the pressure perturbations associated with the shear-layer vorticity mode are expected to dominate.

Defining the directivity of mode (m, n) to be $D_{mn}(\Phi)$ in

$$\tilde{p}_{asm}(\bar{R}, \Phi) = \frac{D_{mn}(\Phi)}{\bar{R}} \exp \left[i\omega\bar{R}\Gamma(\Phi) - im\frac{\pi}{2} \right] \quad (2.40)$$

yields

$$D_{mn}(\Phi) = \frac{\omega(1 - \zeta_o Ma_3)^2 \hat{\eta}^+(\zeta_o)}{\pi H_m^{(1)'}[\kappa_T \omega \sin \Phi / (1 - \kappa_T^2 Ma_3^2 \sin^2 \Phi)^{1/2}] \kappa_T \sin \Phi}. \quad (2.41)$$

This will be used in § 4.5 to calculate the far-field directivity of the scattering mechanisms we evaluate.

Equation (2.40) is identical to corresponding expressions in Munt (1977) and Gabard & Astley (2006), aside from the $\hat{\eta}^+$ term defined in (2.26) that accounts for the different configurations of the respective problems. Moreover, it is easily shown that as $Ma_2 \rightarrow Ma_1$, the $\hat{\eta}^+$ factor of the present work approaches that of Munt (1977). Veitch & Peake (2008) obtain far-field sound from a similar configuration for subsonic core jets, at relatively higher $\omega = 15$, when the buried nozzle, which was explicitly considered in their model, starts to show a significant effect. The frequencies we consider are lower when the rescattering at the buried nozzle could be safely neglected, as required in our model.

3. Linear modes of supersonic shrouded jets

The modes of the shrouded jet configuration of figure 2 are classified here in a broader framework which includes modes that are also present for equivalent free jets, but with an emphasis on the particular phenomenology of modes radiating Mach waves to the far field. This analysis provides a necessary foundation for analysing the mode coupling and scattering at the shroud lip in § 4, which is the main objective of this work. Shrouded jets support a subset of the modes of equivalent free jets that do not strongly interact with the shroud. These modes are principally supported by the core jet and typically change little when solid-wall boundary conditions are imposed on the coflow. In the discussions that follow, these free-jet-like modes are classified along with modes that are unique to the semi-infinite shroud configuration.

For high-Mach-number free jets, the existence of instabilities that do not have counterparts at low Mach numbers is well documented (see Tam & Hu 1989; Luo & Sandham 1997; Parras & Dizes 2010; Nichols & Lele 2011). For free jets with $Ma_1 > 1$, both the branch points ζ_1^\pm are positive (see (2.20a)), which requires the corresponding branch cut to lie on the positive real axis between ζ_1^+ and ζ_1^- . For cold jets with $\kappa_T = 1$, the remaining cuts terminate at $\pm\infty$.

We designate four major types of modes, of which only the fourth (*d*) type corresponds specifically to the semi-infinite shroud configuration.

- (a) *Kelvin–Helmholtz modes.* For a given ω and m , each vortex sheet supports a K–H mode, which in the present classification are the only modes that have incompressible analogues, although their growth rates do vary with compressibility (e.g. Papamoschou & Roshko 1988). For the parameters considered in § 4, where we discuss the lip scattering, the K–H mode on the core jet (figure 3b) has a higher growth rate than the compressibility-coupled

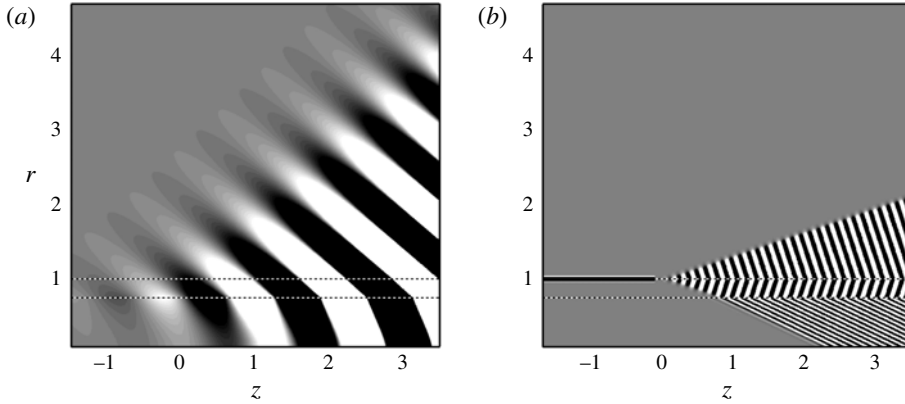


FIGURE 4. The real part of the scattered pressure for incident mode $m = 0$, $\mu_{0n}^+ = -0.847$ for (a) the supersonic jet K–H mode and (b) the subsonic shroud K–H mode for parameters as in figure 3. Grey levels span pressures between ± 0.1 . Dashed lines show the free jet vortex sheets.

instabilities (b), discussed subsequently. Once temperature effects are accounted for, the increased compressibility via heated core jets tends to reduce the growth rates of these modes, as seen in figure 3(c). The K–H mode on the outer shear layer has a still higher growth rate (see figure 3a for the outer K–H mode and compare with the inner one in figure 3b). Moreover, for the case shown, the jet K–H mode has a supersonic phase speed and thus radiates Mach waves, while the subsonic shroud K–H mode is non-radiating, which is clear from the near field of these modes shown in figure 4. The shroud K–H mode (figure 4b), with its subsonic phase speed, has only evanescent pressure waves. However, close to the jet shear layer, these decaying fluctuations dominate the overall pressure fluctuations. In contrast, the jet supersonic K–H mode (e.g. Miles 1957; Ribner 1957) (figure 4a) radiates to the far field. Within the Mach cone, such waves are anticipated to dominate the sound field, which also includes the acoustic waves that these waves are scattered into at the shroud lip, considered in § 4.1. The scattering we consider in § 4 will be an important contributor only outside this region.

- (b) *Supersonic instability modes.* For a vortex sheet model, these modes are predicted to exist for (Tam & Hu 1989)

$$Ma_1 - Ma_2 > \frac{1 + \kappa_T}{\kappa_T}, \tag{3.1}$$

which is satisfied when $\zeta_2^+ > \zeta_1^-$ (see (2.20) and the shaded strip in figure 3b). Figure 3 shows one such case for $\kappa_T = 1$, where the vertical shaded strip satisfies $\zeta_2^+ > \zeta_1^-$, which is where one supersonic instability mode (figure 3b) is seen. This mode is unstable, since $\text{Im}(\zeta) < 0$ indicates spatial growth. The analysis to arrive at (3.1) ignores any azimuthal or radial variation and is thus only valid for $(m, n) = (0, 1)$ (Tam & Hu 1989). General dispersion relations also include these radial wavenumbers (e.g. Samanta & Freund 2008), which depending upon the chosen parameters may result in higher-order modes of successively lower phase speeds and growth rates. Indeed, a second unstable mode is found with

supersonic phase speed, but for $\bar{c} < Ma_2 + 1$, which is inconsistent with the supersonic convection criterion of (3.1) (figure 3*b*). The number of supersonic instability modes increases with the jet Mach number Ma_1 and decreases with the azimuthal mode order m . It should be noted that for heated ($\kappa_T > 1$) jets, conditions like (3.1) could be satisfied at a lower Mach-number difference. For a given $Ma_1 - Ma_2$, this leads to a widening of the shaded strip of figure 3*b*, as shown in figure 3*c*). Like the K–H modes, the growth rates of the supersonic instability modes also reduce with increased κ_T , but there are now modes with subsonic phase speeds which can turn unstable ($\text{Im}(\zeta) < 0$). Figure 5 shows the near field of the two modes with supersonic phase speeds for the parameters of figure 3. The supersonic instability mode in figure 5*a*) has an acoustic near field that resembles the Mach-wave-like radiation of K–H waves, such as seen in figure 4*a*). The associated Mach waves are steeper to the jet shear layer when compared with the K–H mode Mach waves because of their slower phase speed, typical for these modes, but become indistinguishable from the K–H Mach waves for sufficiently high-speed core flows. The supersonic $n = 2$ mode visualised in figure 5*b*) has a still slower phase speed and relatively lower radiation. It will be seen in §4.1 that these instability modes scatter into acoustic waves that are largely confined within the Mach cone, even more so than the scattered acoustic field of the jet K–H mode.

- (c) *Neutral modes.* Similar modes have been identified in free jets (Tam & Hu 1989; Nichols & Lele 2011), where they are termed acoustic since they depend upon finite fluid compressibility, although they have $\text{Im}(\zeta) = 0$ and do not directly generate sound. These are finite in number and can be seen in figure 3*b*). In the present context, these could provide a model for the disturbances created by a fan in the outer flow located upstream. We designate the upstream-phase speed neutral modes as those that have upstream-travelling phase speeds, and *vice versa* for the downstream-phase speed neutral modes. However, both of these have positive group velocities $d\omega/d\mu_{mn} > 0$, so both variants are potentially incident on the shroud lip from within the shroud, as considered in §§4.2 and 4.3.
- (d) *Decaying acoustic modes.* Unlike a free jet, there also exist an infinite number of decaying acoustic modes, which are seen in the upper half-plane of figure 3 with $\text{Im}(\zeta) > 0$. These contribute to the upstream and sideline radiation of shrouded jets, as observed in §4. Corresponding growing acoustic modes, which would be seen in the lower half-plane, do not satisfy the radiation condition.

The flow parameters (see the caption to figure 3) selected for quantifying scattering at the shroud lip in §4 are such that both unstable supersonic and K–H modes are important. The computed maximum spatial growth rates of the axisymmetric unstable supersonic and K–H modes show comparable magnitudes near approximately $Ma_1 = 2.5$ for the Ma_2 , Ma_3 and R as specified in the caption to figure 3. We will particularly focus on a perturbation frequency $\omega = 8$, which corresponds to a Strouhal number $St = fD/U = 0.76$ for core jet Mach number $Ma_1 = 2.5$ and axisymmetric $m = 0$ modes as our baseline configuration, but will also demonstrate in §4.3 that the interactions considered in this work are insensitive to ω . This is because a typical spectrum for high-speed jets has a larger representation from the upstream-phase neutral modes, even for lower coflow magnitudes, like those considered here. Any perturbation frequency ω is therefore more likely to excite a larger fraction of these upstream-phase neutral modes that cause the sideline and upstream acoustic radiation described in §4. At the baseline parameters, the aft Mach-wave radiation is important and a useful comparison with this sideline and upstream radiation is thus possible.

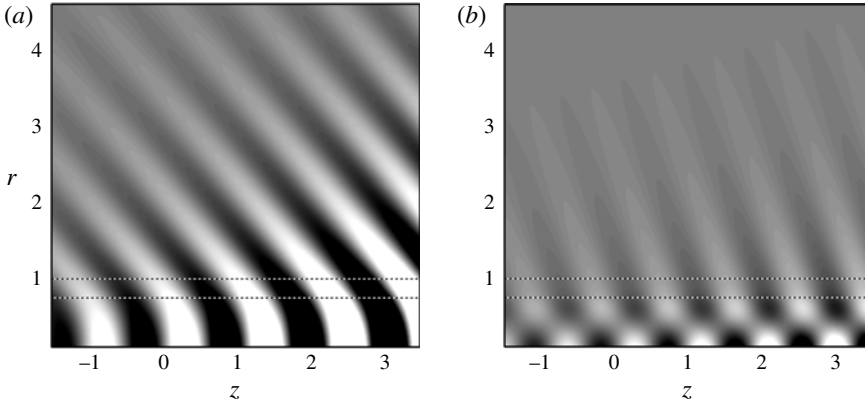


FIGURE 5. The same as figure 4 for (a) a core $n=0$ supersonic instability mode and (b) a higher-order $n=1$ supersonic instability mode.

4. Near-field scattering and far-field sound

For the purpose of comparison, in all cases the net power of the incident wave(s) P_{inc} is taken to be unity at the shroud exit plane $z=0$, which from (2.17) requires

$$P_{inc} = |B^+|^2 \sum_{m=-M}^M \sum_{n=1}^N \int_0^1 |\bar{\Psi}_{mn}(r)|^2 r \, dr = 1, \quad (4.1)$$

where for multimodal incident waves, $\pm M$ and N are the maximum mode numbers of the corresponding azimuthal and radial components, with their respective relative phases being set to zero. In this case, for convenience each of the components is assumed to have equal amplitude, $B_{mn}^+ = B^+$.

4.1. Incident instability modes

Because the turbulence in a jet will have larger associated pressure fluctuations than the acoustic duct modes in the shroud, we first consider the scattering of the instability modes as a phenomenological model for this potentially important interaction. Apart from the core K–H mode, the acoustically coupled supersonic instability mode of the upstream jet is considered for scattering, where the latter has not been studied before. These instability modes are taken to arise from a single downstream-propagating acoustic duct mode scattered at the notional upstream nozzle lip at $z = -L$ (see figure 1) (Samanta & Freund 2008). For the (0, 1) mode with $\mu_{mn}^+ = 0.193$, the resulting incident vorticity mode is visualised in figure 6(a), and the incident supersonic instability mode in figure 7(a) has the form

$$\hat{\phi}_i(r, z) = A_{mn}^+ \omega \Psi_{mn}(r) \exp[i\zeta_{p1} \omega(z - z_L)], \quad (4.2)$$

where ζ_{p1} is a K–H pole of the kernel in (2.22) for the former and a supersonic instability pole for the latter. Thus, $\bar{\Psi}_{mn}(r)$ in (4.1) is

$$|\bar{\Psi}_{mn}(r)|^2 = |A_{mn}^+ \omega \exp(-i\zeta_{p1} \omega z_L) \Psi_{mn}(r)|^2, \quad (4.3)$$

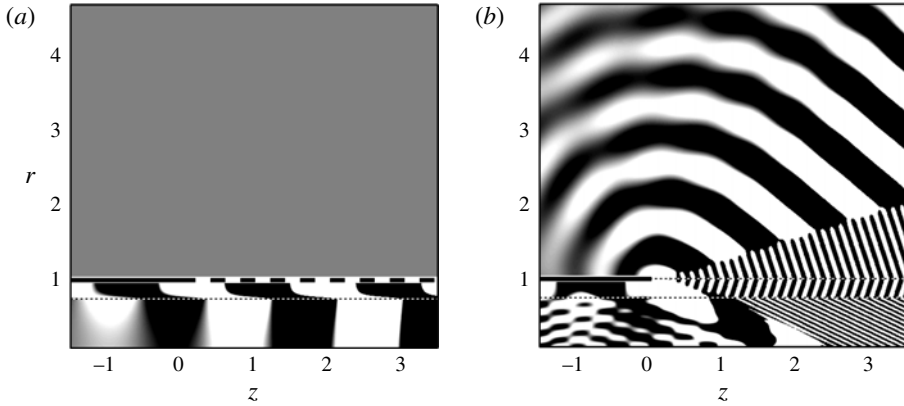


FIGURE 6. The real part of the pressure for (a) the incident vortical perturbation of the core jet shear layer and (b) the total field. The dashed line at $r=1$, $z>0$ represents the confinement of the incident modes inside the shroud. Grey levels span pressures between ± 0.1 . The parameters are $m=0$ and as for figure 3.

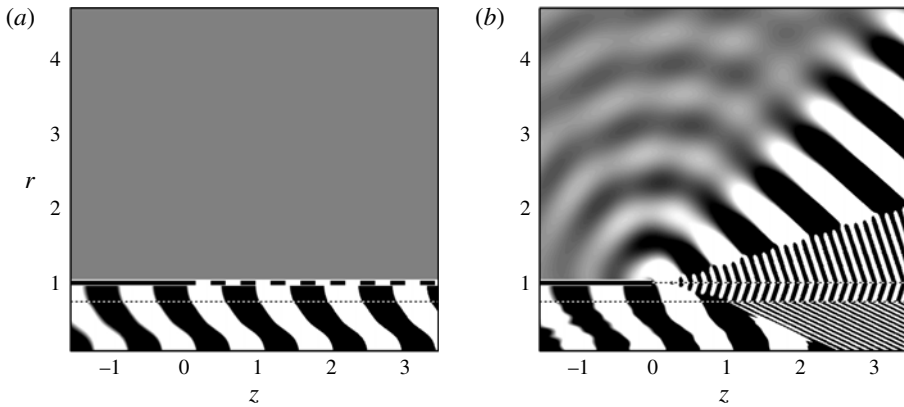


FIGURE 7. The real part of the pressure for the parameters of figure 3: (a) the incident supersonic instability mode of the core jet and (b) the total field. Grey levels span pressures between ± 0.1 .

where A_{mn}^+ is rescaled such that there is unit power at $z=0$. It should be noted that the usual appearance of the K–H mode in figure 6(a) is masked by its relatively long streamwise wavelength compared with the shroud dimensions.

The net scattered pressure fields for the respective modes are shown in figures 6(b) and 7(b). For either incident perturbation, the downstream-directed radiation is dominated, as expected, by the Mach waves arising from the K–H and vorticity-coupled supersonic instability modes. For the incident supersonic instability mode, the acoustic efficiency at sideline and upstream angles drops rapidly and is relatively weak (see also §§ 4.2 and 4.3), while for the incident vorticity mode this is comparable to the broadband results of § 4.3. In any case, given the anticipated strength of the hydrodynamically associated pressure perturbations in either of these incidences, this

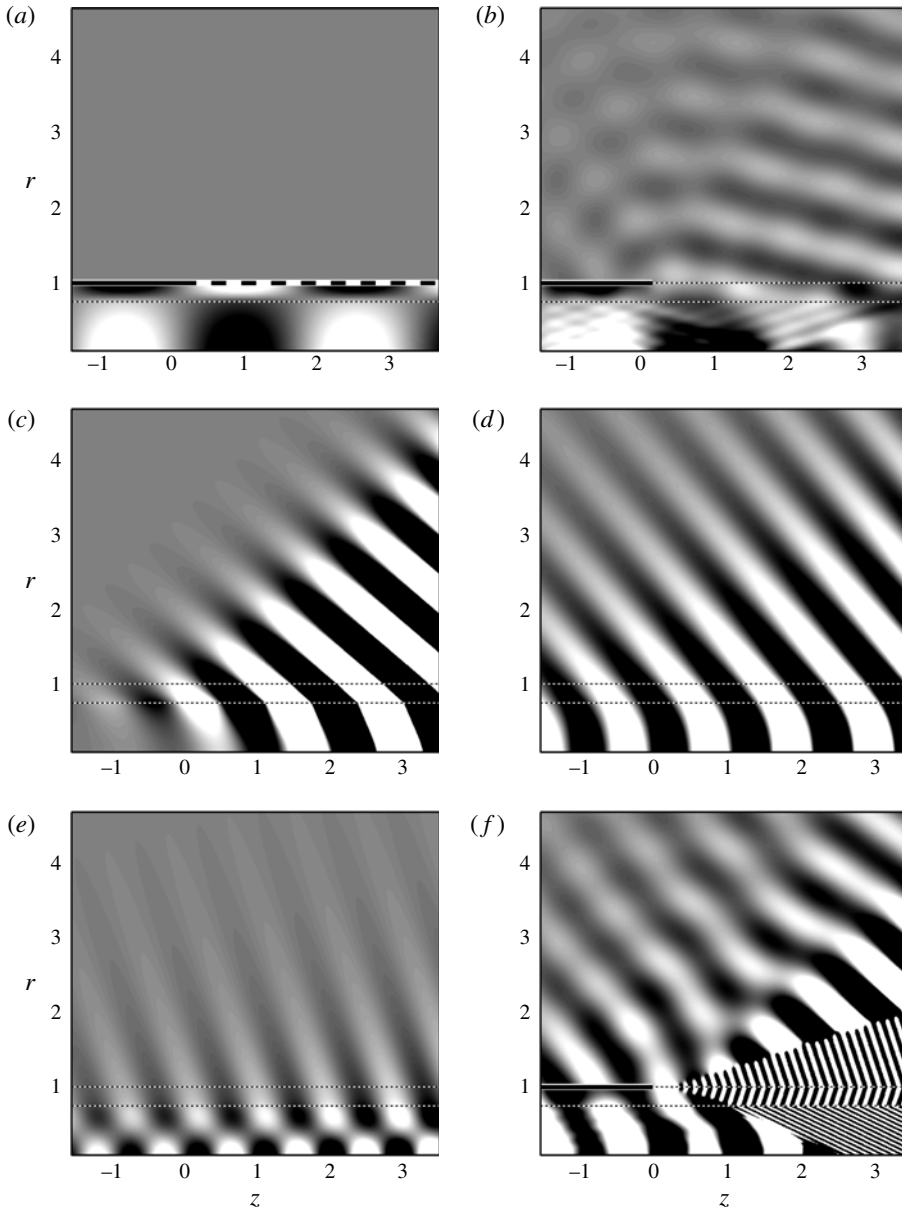


FIGURE 8. The real part of the pressure for the parameters of figure 3: (a) the incident mode with $\mu_{01}^+ = 0.248$, (b) the scattered acoustic modes, (c) the scattered jet K-H mode, (d) the scattered $n = 1$ supersonic instability mode, (e) the scattered $n > 1$ supersonic instability mode and (f) the total field. Grey levels span pressures between ± 0.8 .

is potentially an important noise source in these directions. The scattering of incident acoustic modes, which we consider next, will be found to be more efficient, especially when compared with the supersonic instability mode, in the sideline and upstream directions, but is not anticipated to necessarily be of comparable incident amplitudes in most practical configurations unless coupled to a hydrodynamic source mechanism.

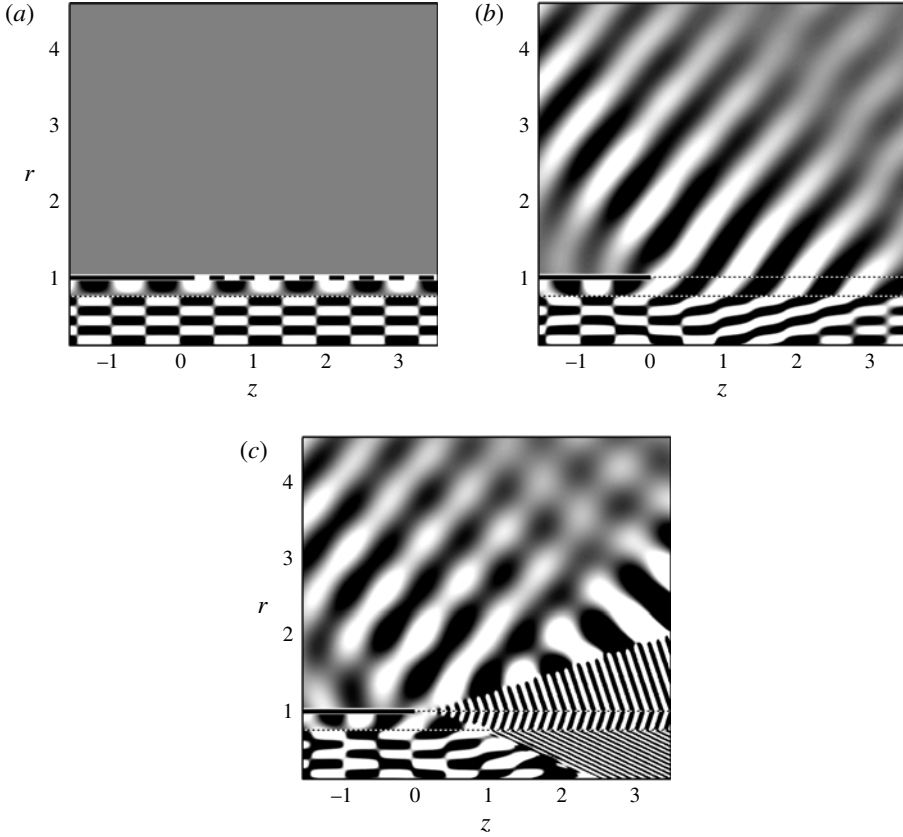


FIGURE 9. The real part of the pressure for the parameters of figure 3: (a) the incident mode with $\mu_{06}^+ = -0.847$, (b) the scattered acoustic modes and (c) the total field. Grey levels span pressures between ± 0.1 .

4.2. Incident duct modes

From (2.17), the incident duct modes are

$$\hat{\phi}_i(r, z) = B_{mn}^+ \Psi_{mn}(r) \exp(i\mu_{mn}^+ \omega z), \quad (4.4)$$

where μ_{mn}^+ is the wavenumber of a particular right-running mode with shape $\Psi_{mn}(r)$. The specific expressions match those in the subsonic limit (Samanta & Freund 2008). In (4.4), B_{mn}^+ is chosen according to (4.1), so that $|\bar{\Psi}_{mn}(r)|^2 = |\Psi_{mn}(r)|^2$.

We consider $m = 0$ waves, which for the conditions in figure 3 support seven right-propagating incident modes: $n = 1, 2, \dots, 7$. Figure 8(a) shows the incident wave $(m, n) = (0, 1)$, where $\mu_{01}^+ = 0.248$, and figure 8(b–e) shows the scattered waves. Figure 8(f) shows the net scattered pressure including the contribution from the scattered shroud K–H mode. The sound is predominantly directed aftward (lower Φ) in a Mach cone.

A very different behaviour is seen in figure 9(b), for the $(0, 6)$ incident mode with $\mu_{06}^+ = -0.847$ (figure 9a), which has a negative phase speed but positive group velocity. In this case, the radiation is mainly upstream. The scattered K–H and supersonic

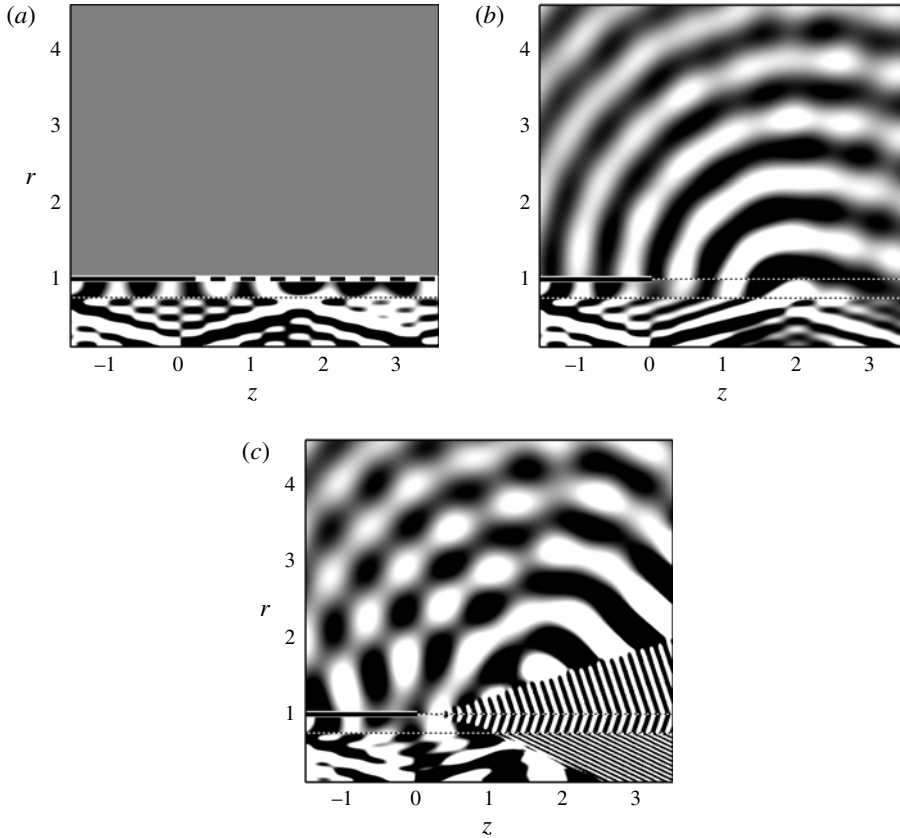


FIGURE 10. The real part of the pressure for a multimode case composed of $\sum_1^7(0, n) = 7$ incident duct modes. Grey levels span pressures between ± 0.1 . The parameters match those of figure 3: (a) incident; (b) scattered acoustic; (c) total.

instability modes (figures 4 and 5) are qualitatively similar to the (0, 1) incident case of figure 8 but are of comparable magnitude to the scattered acoustic pressure, which is also apparent in the total pressure contours of figure 9(c).

4.3. Incident broadband duct modes

The tonal incident acoustic modes considered in § 4.2 can be efficient, but modern fan designs avoid significant tones. A broadband noise source mechanism is more representative of the pressure perturbations generated mainly due to the interactions between the fan blade turbulent wakes and stator surfaces, and between the blade tips and the casing boundary layer (Peake & Parry 2012). In this case, using (2.17) with the amplitudes of each of the component modes B_{mn}^+ equal, such that $B_{mn}^+ = B^+$, yields unit incident power via (4.1).

Figures 10 and 11 show two examples. For the parameters of figure 3, a total of 103 propagating neutral modes are possible, which on considering azimuthal symmetry reduces to 55 distinct modes. Figure 10 shows the case where the multimode incident wave of figure 10(a) is composed of all seven axisymmetric $m = 0$ modes. The scattered acoustic pressure has a significant upstream contribution, as seen in figure 10(b). It is comparable to the downstream Mach radiation, as visible

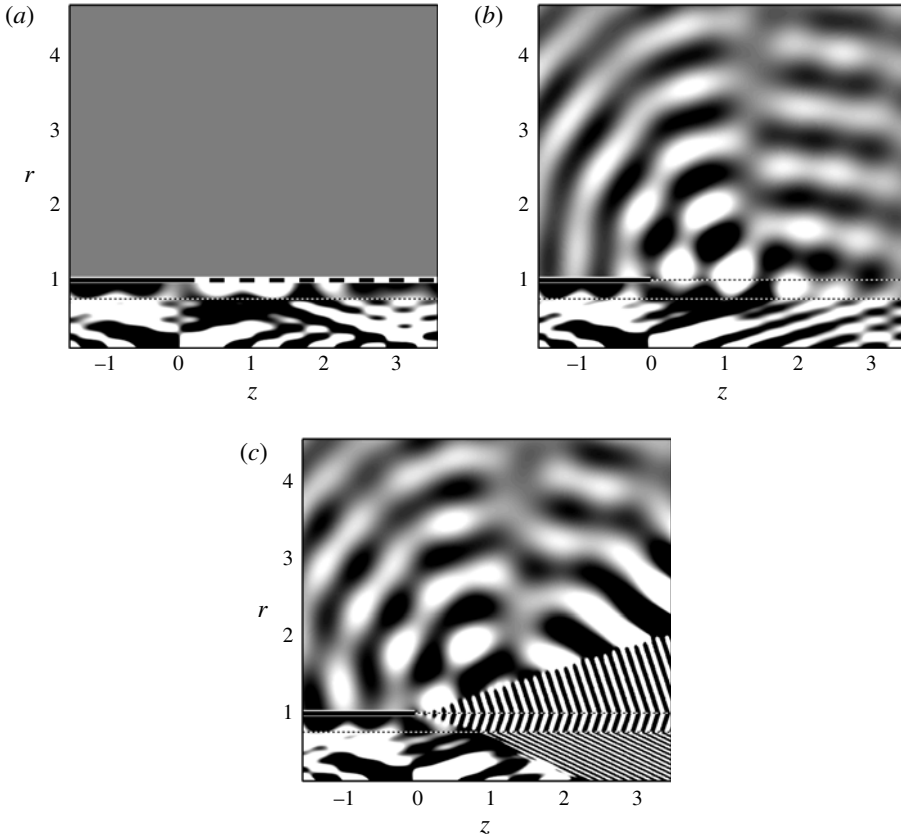


FIGURE 11. The same as figure 10, but supporting $\sum_{-4}^4 \sum_n(m, n) = 47$ incident duct modes: (a) incident; (b) scattered acoustic; (c) total.

in the total field of figure 10(c). In the second example, figure 11 shows the same when the incident mode of figure 11(a) has a higher modal content: the first 47 modes (up to $m = \pm 4$). A broadband source seems to progressively smooth out the strong directional radiation seen in the tonal sources. The radiation is also increasingly upstream directed with increased incident modal content, a direct consequence of a high-speed core jet ejecting into a low subsonic coflow, which supports a relatively broad spectrum of upstream-phase speed neutral modes supported by the flow. It should be noted that in both cases the wave field inside the shroud is essentially unaltered by the scattering, which supports neglect of upstream reflections off the buried-nozzle lip for our chosen parameters. The periodic cross-hatched patterns seen inside the core jets (see especially figures 10b, 11b) indicate acoustic waves trapped inside the jet, repeatedly reflecting off the cylindrical shear layer.

Whether such upstream radiation of figures 10(b) and 11(b) is typical of high-speed jets as considered here and whether such results are independent of the perturbation frequency ω is investigated by considering several incident ω cases in figure 12: $\omega = 4$ (figure 12a,b), $\omega = 6$ (figure 12c,d) and $\omega = 10$ (figure 12e,f). In each case, only the axisymmetric $m = 0$ multimode scattering results are shown. The scattered acoustic pressure in each case has a strong sideline and upstream component similar to the $\omega = 8$ baseline case and confirming frequency insensitivity for the configuration we consider.

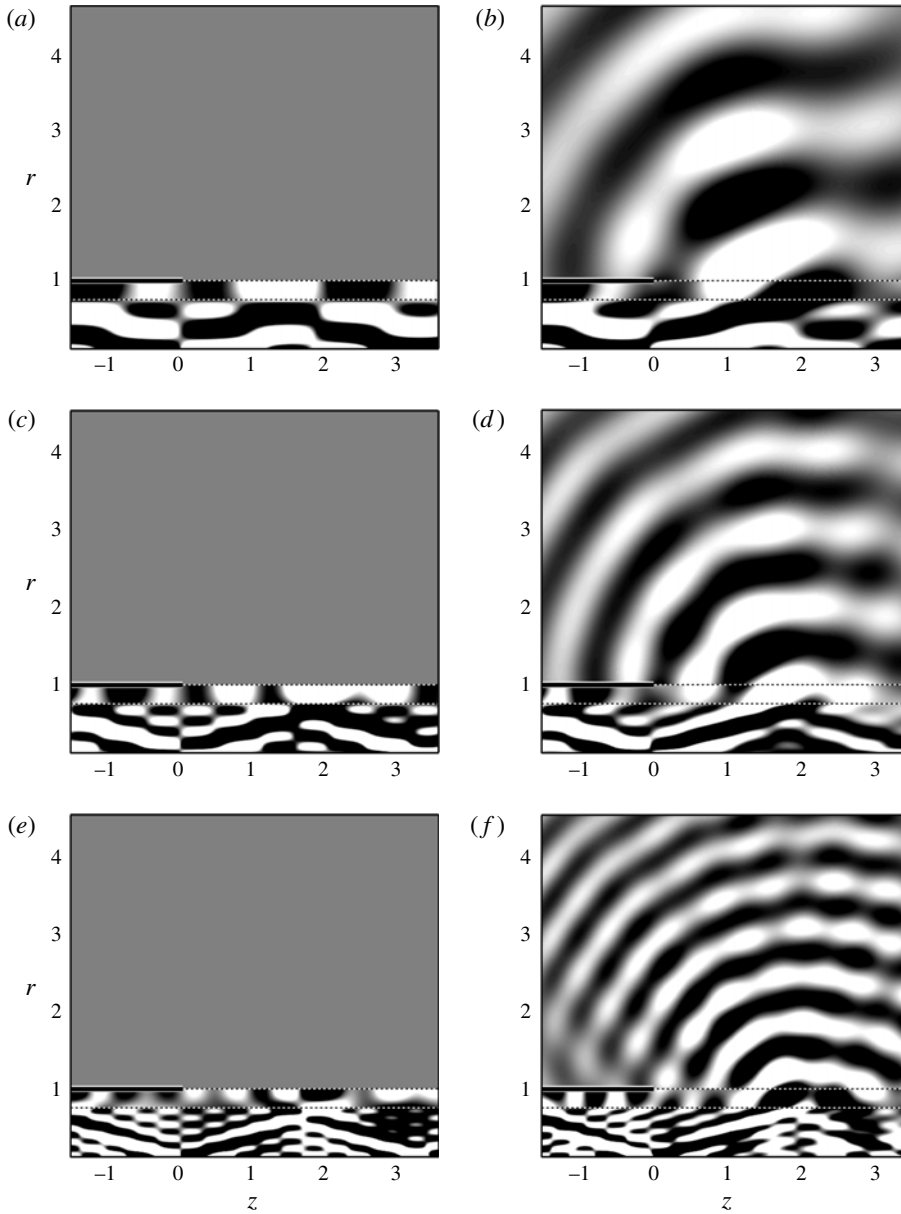


FIGURE 12. The real part of the pressure for a multimode incident case composed of all the $m=0$ symmetric incident duct modes at perturbation frequencies of (a,b) $\omega = 4$, (c,d) $\omega = 6$ and (e,f) $\omega = 10$ ((a,c,e) incident and (b,d,f) scattered acoustic). Grey levels span pressures between ± 0.1 . The other parameters match those of figure 3.

4.4. Comment on the sound source

An interesting feature of the acoustic scattering observed in the cases considered here is the apparent extent of the acoustic source several diameters downstream of the shroud exit, as clearly seen in figures 8(b), 9(b), 10(b) and 11(b). Here, the dominant radiation directions depend upon the respective phase speeds of the incident mode(s).

For example, for the case considered in figure 9, the phase speed of the incident tonal acoustic wave is negative, which results in a predominantly upstream acoustic radiation with a peak at $\Phi = 138^\circ$. In figure 10(b), the apparent source of upstream-propagating sound appears to be at one jet diameter downstream rather than near the shroud itself. This downstream extent of the acoustic source is related to the relative magnitudes of the core jet Mach number Ma_1 and of the coflows. Specifically, for the configuration considered here, this extent is inversely proportional to $(\zeta_1^+ - \zeta_3^-)$, the difference between the positive branch point corresponding to Ma_1 and the negative branch point corresponding to Ma_3 , whose specific forms appear in (2.20). For the same $Ma_3 = 0.1$ as considered here but with a subsonic core jet, this difference is larger as ζ_1^+ is inversely proportional to Ma_1 . This results in a faster decay and thus a shorter streamwise extent of the acoustic source (see figure 8b of Samanta & Freund 2008) than observed for the supersonic cases considered here.

4.5. Far-field sound

The far-field directivity for the incident modes is shown in figure 13. For the single-mode tonal scattering (figure 13a), the respective downstream and upstream peaks of the (0, 1) and (0, 6) incident modes reflect the most intense radiation directions of figures 8(b) and 9(b) respectively. The radiated sound from the multimode incident waves (figure 13a) is sideline and upstream biased, most closely resembling that for the upstream-phase speed incident mode case. For the axisymmetric seven-mode incident case, each of the undulations in the flatter sideline region of the directivity corresponds to the individual tonal peaks, albeit with reduced magnitudes. The 47-mode scattering essentially results in approximately uniform directivity for $\Phi > 70^\circ$. In general, multimode radiation patterns are smoother because of averaging and mostly sideline and upstream oriented because of a presence of the upstream-phase speed modal content in the incident wave field. In figure 13(b), the radiation of the scattered K–H mode is more intense downstream, though comparable (although not uniformly so) to the 47-mode multimode pressure upstream. The supersonic instability mode, being acoustically coupled, scatters most efficiently into acoustic and Mach waves within the Mach cone (figure 13b). The sideline and upstream radiation is significantly less efficient than the scattered K–H mode and the broadband acoustic modes.

Figure 13(c) shows that the sideline and upstream radiation of the multimodal waves is insensitive to the perturbation frequency for the values of $\omega = 2, 4, 6, 8, 10$ considered here. All of the corresponding axisymmetric $m = 0$ multimode radiations seem to fall within a band of ± 5 dB.

4.6. Sensitivity to the Kutta condition

It is theoretically possible to alter the radiated sound by modifying the geometry of the shroud edge, which alters the strength of the shroud vortical mode (Bechert 1980). This is explored here indirectly through variation of α in (2.26), which modifies the shroud-lip Kutta condition. We consider two cases: $\alpha = 1$ corresponds to the full-vortex-shedding case, with all the available vorticity shed from the shroud lip, and $\alpha = 0$ suppresses vortex shedding, but ignores any phase of α . The role of vortex shedding has been shown to be significant at lower ($\omega \rightarrow 0$) frequencies and especially for plane waves (Rienstra 1983, 2007), but for the parameters considered here ($\omega = 8$) and as seen in figure 13(d), such variations have little influence for tonal and K–H mode scattering. These results would be similar even for shroud walls coated with compliant

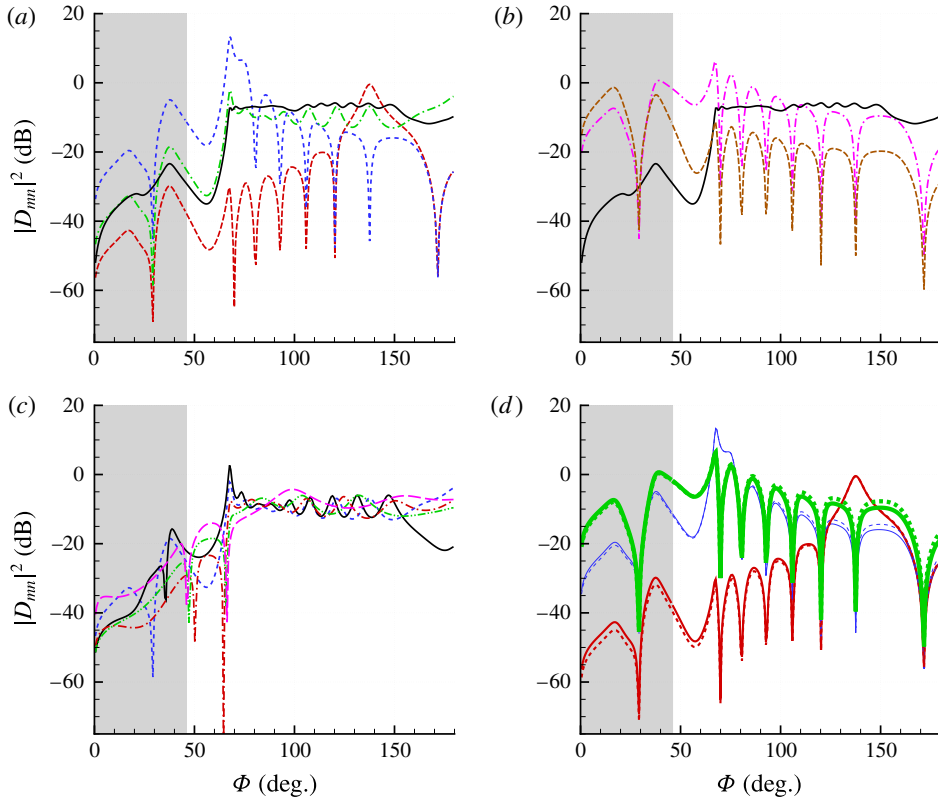


FIGURE 13. (Colour online) The far-field sound pressure for (a) different incident tonal and broadband duct modes: --- (0, 1) downstream-phase speed tonal; ——— (0, 6) upstream-phase speed tonal; — · — $\sum_n(0, n)$ seven-mode multimodal; ——— $\sum_{-4}^4 \sum_n(m, n)$ 47-mode multimodal; and (b) different incident instability modes: — · — K–H; ——— supersonic instability; ——— $\sum_{-4}^4 \sum_n(m, n)$ 47-mode multimodal. (c) The far-field sound pressure for $\sum_n(0, n)$ multimodal axisymmetric at ——— $\omega = 10$; --- $\omega = 8$; — · — $\omega = 6$; — · · — $\omega = 4$; ——— $\omega = 2$. (d) The effect of vortex shedding per the selected Kutta condition for (normal lines) (0, 6) upstream-phase speed acoustic; (thinner lines) (0, 1) downstream-phase speed acoustic; (thicker lines) K–H incidence with ——— $\alpha = 1$ and --- $\alpha = 0$. The shaded grey band (up to $\Phi = 46^\circ$) represents the zone-of-influence of the axisymmetric $m = 0$ instability modes defined in (2.39). The other parameters are the same as for figure 3.

liners (Brambley 2009b). For the downstream-phase speed (0, 1) mode incidence there is at most an ~ 1 dB change along the forward arc, for the upstream-phase speed (0, 6) mode there appears to be an ~ 0.5 dB difference in the rearward arc, while for the incident vorticity mode there is an ~ 2 dB difference in the forward arc.

5. Conclusions

The main conclusion is that shrouded isothermal supersonic jets, like those we consider here as a model for buried-nozzle turbofan engines, have the potential to generate strong sideline and upstream sound radiation via scattering of incident acoustic and instability modes at the shroud lip. At these angles, this is comparable

to the sound generated by the Mach waves of the instabilities that are spawned. Depending upon the mix of hydrodynamic and broadband acoustic modes, such radiation could constitute the primarily upstream sound over a broad range of sideline and forward angles. Because of the different coflow speeds and the varying phase speeds of the underlying modes, some of this radiation appears to originate a full jet diameter downstream of the shroud lip for the parameters we consider.

Acknowledgements

A.S. gratefully acknowledges the IISc startup grant (11-0501-0541-01-403), the MHRD–GARP (CPDA grant no. 0110051958) and the ISRO–IISc STC (ISTC/MAE/AS/296) for support. J.B.F. gratefully acknowledges support of the US Office of Naval Research (N00014-11-1-0756) and the US AFOSR (no. FA9550-10-1-0432).

REFERENCES

- ABRAMOWITZ, M. & STEGUN, I. A. 1964 *Handbook of Mathematical Functions with Formulas, Graphs, and Mathematical Tables*, National Bureau of Standards Applied Mathematics Series, vol. 55. US Government Printing Office.
- BECHERT, D. 1980 Sound absorption caused by vorticity shedding, demonstrated with a jet flow. *J. Sound Vib.* **70** (3), 389–405.
- BRAMBLEY, E. J. 2009a Fundamental problems with the model of uniform flow over acoustic linings. *J. Sound Vib.* **322**, 1026–1037.
- BRAMBLEY, E. J. 2009b Low-frequency acoustic reflection at a hard–soft lining transition in a cylindrical duct with uniform flow. *J. Engng Maths* **65** (4), 345–354.
- CHU, B. & KOVASZNY, L. S. G. 1957 Nonlinear interactions in a viscous, heat-conducting, compressible gas. *J. Fluid Mech.* **3**, 494–514.
- CRIGHTON, D. G. & HUERRE, P. 1990 Shear-layer pressure fluctuations and superdirective acoustic sources. *J. Fluid Mech.* **220**, 355–368.
- CRIGHTON, D. G. & LEPPINGTON, F. G. 1974 Radiation properties of the semi-infinite vortex sheet: the initial-value problem. *J. Fluid Mech.* **64** (2), 393–414.
- GABARD, G. & ASTLEY, R. J. 2006 Theoretical model for sound radiation from annular jet pipes: far- and near-field solutions. *J. Fluid Mech.* **549**, 315–341.
- GILL, A. E. 1965 Instabilities of top-hat jets and wakes in compressible fluids. *Phys. Fluids* **8**, 1428–1430.
- HARPER-BOURNE, M. & FISHER, M. J. 1973 The noise from shock waves in supersonic jets. In *Proceedings of the AGARD Conference on Noise Mechanisms*, CP-131. AGARD, pp. 11,1–13.
- HEATON, C. J. & PEAKE, N. 2006 Algebraic and exponential instability of inviscid swirling flow. *J. Fluid Mech.* **565**, 279–318.
- HIRSCHBERG, A. & HOEIJMAKERS, M. 2014 Comments on the low frequency radiation impedance of a duct exhausting a hot gas. *J. Acoust. Soc. Am.* **136** (2), EL84–EL89.
- HO, C. M. & HUERRE, P. 1984 Perturbed free shear layers. *Annu. Rev. Fluid Mech.* **16**, 365–424.
- JONES, D. S. & MORGAN, J. D. 1974 A linear model of a finite amplitude Helmholtz instability. *Proc. R. Soc. Lond. A* **338**, 17–41.
- JORDAN, P. & COLONIUS, T. 2013 Wave packets and turbulent jet noise. *Annu. Rev. Fluid Mech.* **45**, 173–195.
- LAUFER, J. & YEN, T. 1983 Noise generation by a low-Mach number jet. *J. Fluid Mech.* **134**, 1–31.
- LEVINE, H. & SCHWINGER, J. 1948 On the radiation of sound from an unflanged circular pipe. *Phys. Rev.* **73** (4), 383–406.
- LIU, J. T. C. 1981 Interaction between large-scale coherent structures and fine-grained turbulence in free shear flows. In *Transition and Turbulence*, Proceedings of the Symposium on Transition and Turbulence in Fluids, Madison, WI, October 13–15, 1980, pp. 167–214. Academic.

- LUO, K. H. & SANDHAM, N. D. 1997 Instability of vortical and acoustic modes in supersonic round jets. *Phys. Fluids* **9** (4), 1003–1013.
- MICHALKE, A. 1972 The instability of free shear layers. *Prog. Aerosp. Sci.* **12**, 213–239.
- MILES, J. W. 1957 On the reflection of sound at an interface of relative motion. *J. Acoust. Soc. Am.* **29** (2), 226–228.
- MORGAN, J. D. 1974 The interaction of sound with a semi-infinite vortex sheet. *Q. J. Mech. Appl. Maths* **27** (4), 465–487.
- MUNT, R. M. 1977 The interaction of sound with subsonic jet issuing from a semi-infinite cylindrical pipe. *J. Fluid Mech.* **83**, 609–640.
- MUNT, R. M. 1990 Acoustic transmission properties of a jet pipe with subsonic jet flow: I. The cold jet reflection coefficient. *J. Sound Vib.* **142** (3), 413–436.
- NICHOLS, J. W. & LELE, S. K. 2011 Global modes and transient response of a cold supersonic jet. *J. Fluid Mech.* **669**, 225–241.
- NOBLE, B. 1988 *Methods Based on The Wiener–Hopf Technique*, 2nd edn. Chelsea.
- ORSZAG, S. A. & CROW, S. C. 1970 Instability of a vortex sheet leaving a semi-infinite plate. *Stud. Appl. Maths* **49** (2), 167–181.
- PAPAMOSCHOU, D. & DEBIASI, M. 2003 Conceptual development of quiet turbofan engines for supersonic aircraft. *J. Propul. Power* **19** (2), 161–169.
- PAPAMOSCHOU, D. & ROSHKO, A. 1988 The compressible turbulent shear layer: an experimental study. *J. Fluid Mech.* **197**, 453–477.
- PARRAS, L. & DIZES, S. L. 2010 Temporal instability modes of supersonic round jets. *J. Fluid Mech.* **662**, 173–196.
- PEAKE, N. 1994 The viscous interaction between sound waves and the trailing edge of a supersonic splitter plate. *J. Fluid Mech.* **264**, 321–342.
- PEAKE, N. & PARRY, A. B. 2012 Modern challenges facing turbomachinery aeroacoustics. *Annu. Rev. Fluid Mech.* **44**, 227–248.
- POWELL, A. 1953 On the mechanism of choked jet noise. *Proc. Phys. Soc. B* **66**, 1039–1056.
- RIBNER, H. S. 1957 Reflection, transmission and amplification of sound by a moving medium. *J. Acoust. Soc. Am.* **29** (4), 435–441.
- RIENSTRA, S. W. 1983 A small Strouhal number analysis for acoustic wave-jet flow-pipe interaction. *J. Sound Vib.* **86** (4), 539–556.
- RIENSTRA, S. W. 1984 Acoustic radiation from a semi-infinite annular duct in a uniform subsonic mean flow. *J. Sound Vib.* **94** (2), 267–288.
- RIENSTRA, S. W. 2007 Acoustic scattering at a hard–soft lining transition in a flow duct. *J. Engng Maths* **59** (4), 451–475.
- SAMANTA, A. 2009 Finite-wavelength scattering of incident vorticity and acoustic waves at a shrouded-jet exit. PhD thesis, University of Illinois at Urbana-Champaign.
- SAMANTA, A. & FREUND, J. B. 2008 Finite-wavelength scattering of incident vorticity and acoustic waves at a shrouded-jet exit. *J. Fluid Mech.* **612**, 407–438.
- SHEN, H. & TAM, C. K. W. 2002 Three-dimensional numerical simulation of the jet screech phenomenon. *AIAA J.* **40** (1), 33–41.
- SMITH, M. J. T. 2004 *Aircraft Noise*. Cambridge University Press.
- TAM, C. K. W. 1995 Supersonic jet noise. *Annu. Rev. Fluid Mech.* **27**, 17–43.
- TAM, C. K. W. 2009 Mach wave radiation from high-speed jets. *AIAA J.* **47** (10), 2440–2448.
- TAM, C. K. W., GOLEBIEWSKI, M. & SEINER, J. M. 1996 On the two components of turbulent mixing noise from supersonic jets. *AIAA Paper* 96-1716.
- TAM, C. K. W. & HU, F. Q. 1989 On the three families of instability waves of high-speed jets. *J. Fluid Mech.* **201**, 447–483.
- TAM, C. K. W., PARRISH, S. A. & VISWANATHAN, K. 2014 Harmonics of jet screech tones. *AIAA J.* **52** (11), 2471–2479.
- TAYLOR, M. V., CRIGHTON, D. G. & CARGILL, A. M. 1993 The low frequency aeroacoustics of buried nozzle systems. *J. Sound Vib.* **163** (3), 493–526.
- VEITCH, B. & PEAKE, N. 2008 Acoustic propagation and scattering in the exhaust flow from coaxial cylinders. *J. Fluid Mech.* **613**, 275–307.